JGR Oceans

RESEARCH ARTICLE
10.1029/2021JC017669

Free Wave Effects in Meteotsunamis

John Grue[1], Geir K. Pedersen[1], and Øyvind Saetra[2]

[1]Department of Mathematics, Section for Mechanics, University of Oslo, Oslo, Norway, [2]Division for Ocean and Ice, Norwegian Meteorological Institute, Oslo, Norway

Key Points:

- Foreward running waves are generated by ships and storms moving across great depth changes of the water
- The forced wave and velocity field attached to the moving pressure system are modified at the depth change, generating the waves
- Short waves are generated by the strong gradients of the pressure system

Correspondence to:

J. Grue,
johng@math.uio.no

Citation:

Grue, J., Pedersen, G. K., & Saetra, Ø. (2022). Free wave effects in meteotsunamis. *Journal of Geophysical Research: Oceans*, *127*, e2021JC017669. https://doi.org/10.1029/2021JC017669

Received 11 JUN 2021
Accepted 16 NOV 2021

Abstract Free wave generation due to a ship or storm moving past a shallow, great depth change of the water, is measured on the shore (coast), modeled and compared. The free waves are generated at the depth change where the forced wave and velocity field attached to the moving pressure system adjust to the new depth. The wavenumber is a factor 1/12 smaller in the meteotsunami case compared to the ship case. The subcritical depth Froude numbers are similar in the two cases. The meteotsunami that occurred on the Norwegian Coast on 29–30 June 2019 was driven by a supercell thunderstorm moving at speed 110 km/hr. A localized, strong high pressure feature of width of 60 km and crest of 120 km obtained from weather forecast was used as input for a set of simulations of the water-level response including realistic bathymetry. At the transition between the North Sea and the Norwegian Trench, the storm generated a free depression wave. This arrived at the coast 24 min ahead of the depression attached to the storm. The calculation fits to a period of 23 min, of a series several oscillations of height of 0.3–0.4 m, as measured by the water-level gauge. An impulsive start-up generates an additional forerunning elevation wave. Short waves of period of 1/3 of the main ship-driven waves may originate from the steep gradients of the bow and stern. Similarly, short waves of period 6–7.5 min (0.002–0.003 Hz) are observed in the measured water-level on the coast.

Plain Language Summary Small tsunamis are caused similarly by ships and storms as they move past great, shallow depth changes of the water. The waves move upstream of the source. The small ship tsunamis are a recent phenomenon in the shallow water ways of Oslofjorden, Norway, where Color Fantasy and Color Magic, the world's largest cruiseferries with a car deck, introduced in 2004 and 2007, respectively, make the 0.5–1 km long waves. The similar wave generation happened in a recent meteotsunami on the Norwegian Coast on 29–30 June 2019. A supercell tunderstorm moving at speed 110 km/hr across the shallow North Sea generated a forward running 50 km long depression wave at the transition to the deep Norwegian Trench. The forerunning free wave arrived at the coast 24 min ahead of the wave attached to the storm. The combination of the waves generated resonant oscillations in the coastal waters, as measured by water-level gauges. The tsunamis cause erosion and damage on the coast. The ship- and meteotsunamis share several similarities. The ship's bow and stern may generate shorter waves, in addition to the long waves. Similar short waves, measured in the meteotsunami case, fit with the infra gravity wave range.

1. Introduction

Meteorological (meteo-) tsunamis are long ocean surface waves caused by weather events (e.g., Monserrat et al., 2006; Pattiaratchi & Wijeratne, 2015). Typical period of the waves is in the range from 1 min to 2 hr. The waves are generated by the strong gradients of the wind or pressure system and depend on the speed of the atmospheric disturbance. Wave magnification may occur when the speed corresponds to the shallow water speed, referred to as Proudman resonance (e.g., Mercer et al., 2002; Niu & Zhou, 2015). Wave shoaling and resonance with the topography of the coast may further enhance the elevation (e.g., Chen & Niu, 2018; Šepić et al., 2018). A description of meteotsunami events occurring in various parts of the world may be found in Monserrat et al. (2006). Recently, a review on meteotsunamis (Rabinovich, 2020) and a special issue on the global perspective on meteotsunami science (Vilibić et al., 2021) were published. Definitions, generation, and propagation characteristics of seismic tsunamis, storm surges, and meteotsunamis were compared by Pattiaratchi and Wijeratne (2015). They list sources from above the sea surface, including the inverse barometer consequence coupled with resonance effects. The source extent is characterized as over the region, where the build-up period takes place during hours.

Free wave effects appear not to be appreciated in the literature of meteotsunamis. However, free gravity waves have been found to be emitted by storms passing by substantial depth changes of the ocean (Vennell, 2007). Here,

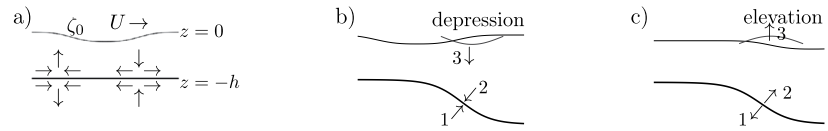

Figure 1. (a) Free wave generation by depression ζ_0 moving at speed U across a localized, great depth increase. Fluid velocity arrows at a flat bottom. (b) The front face of the depression produces a normal velocity arrow 1 at the depth increase. This produces reaction velocity arrow 2 at the impenetrable bottom. This velocity vector appears as a vertical velocity arrow 3 at the free surface, producing a depression. (c) Velocity arrows are reversed at the trailing part, producing an elevation.

we investigate how free wave effects were part of a recent meteotsunami that occurred on the coast of Norway as well. On 29–30 June 2019 a strong, localized high pressure feature was moving across the shallow North Sea. The Froude number was larger than 0.85. The storm eventually moved across the deep Norwegian Trench before arriving at the coast in the morning of 30 June. The weather caused oscillations of up to 0.8 m of the water level in fjords, lasting for about a day. Eyewitnesses living in Byrknes on the Norwegian coast reported on the violent long wave event. This started on 03:30 in the morning of 30 June, lasting for a few hours (H. Svanholm, B.G. Misje, 2020; personal communication). Piers, undamaged ever since they were built in the 1950s, were washed away. Norwegian Authorities were unable to connect any cause to the event. Hence, insurance claims were declined, as reported by the Norwegian Broadcasting on 24 February 2020. Water level recordings at the specific location of Byrknes on the coast, made available from Norwegian Mapping Authority, show that the elevation went from a calm to fluctuating state in the evening of 29 June, and that relatively regular oscillations occurred in the morning of 30 June (Figure 3e). The oscillation period of barely 0.4 hr cannot be explained by just the barometer effect of the moving storm. We investigate how free, long gravity waves of essential amplitude contributed to the meteotsunami event, in addition to the forced wave.

Free waves in meteotsunamis may originate similarly as the ship-driven mini-tsunamis in the shallow waterways of the Oslofjorden, Norway, where the waves appear at the shallow, great depth changes of the water (Grue, 2017, 2020). The mechanism is as follows. Moving along a flat bottom, a forced flow field is attached to the pressure system (ship). At a localized depth change, the forced flow adjusts to the new depth. This is where the free wave generation happens. To illustrate the process, let ζ_0 denote the forced elevation. A corresponding vertical fluid velocity is forced below the moving pressure system: $w \simeq -U(\partial\zeta_0/\partial x)(1 + z/h)$ (U motion speed, x coordinate along the motion direction, z vertical coordinate with $z = 0$ at the surface, h water depth). Similar horizontal velocities (u, v) are induced. In the case of a depression, the vertical fluid velocity is negative at the front face of ζ_0. A vertical image velocity below the bottom is positive (Figure 1a). At a depth increase, the velocity vector induced by the moving pressure distribution, indicated by arrows 1 in Figures 1b and 1c, produces a reaction velocity (the term "reaction velocity," suggested by Grue, 2020, is a direct interpretation of Equation 3 in Section 2.2 below) of equal magnitude and opposite direction, orthogonal to the impenetrable bottom, at its new level. This is indicated by arrows 2 in Figures 1b and 1c and causes a vertical velocity at the water surface, indicated by arrows 3 in Figures 1b and 1c. Free waves are then generated. The generation process takes place during the period when the forced flow relaxes to the new depth. This relaxation period needs to be calculated. The process follows the mathematical arguments by Grue (2020), and the generation process described here includes the patching technique valid in the long wave regime derived by Vennell (2007). The free wave generation mechanism, at a great depth change, in the two different applications (ship hydrodynamics or meteotsunamis) was derived independently. We note that a sudden start-up of from rest at constant depth is another source of free wave transients, both for the ship case and the meteotsunami case (e.g., Dogan et al., 2021, their Equation 19), where such free wave effects are evidenced in the storm investigated here.

In the sense that the free waves are generated by a transient vertical velocity of the water surface, and the wave making process discussed here is similar to that of tectonic tsunamis (e.g., Satake & Atwater, 2007). However, the analogy is even closer with waves generated by underwater mass failures (e.g., Didenkulova et al., 2010; Tinti et al., 2001) or and land-slides (e.g., Løvholt et al., 2015). Although length and time scales are different in the various cases, there are close analogies between the meteotsunamis, ship-generated waves, and the waves generated by slides.

The aim of the present paper is to illustrate the free wave generation process caused by a pressure system moving past a localized, great depth change where $\Delta h/h = O(1)$. We connect observations and calculations of two cases

(ship and meteotsunami) where this kind of wave generation has been taking place. We emphasise that the wave generation investigated here occurs at a subcritical speed. This is characterized by the Froude number defined by $Fr = U/\sqrt{gh}$, where U is the speed of the disturbance, g is the acceleration of gravity, and $\sqrt{gh}$ is the shallow water speed. As regards the ship-driven waves presented here, the Froude number is up to 0.85 ($U = 10$ m/s) above the shallow region where the waves are generated, where the local water depth is reduced to 14 m over a short distance. The local Froude number is up to 0.96 for the greatest speed of 11.3 ms^{-1} in one case. However, nonlinear calculations of the ship case, to be presented elsewhere, do neither show a bow wave, nor a modification of the upstream wave generation, for the subcritical Froude number range, over the short traveling distance investigated here. However, the effect of the depth change is at work in the present cases. In the calculations of the meteotsunami that occurred on 29–30 June 2019, the Froude number was up to 0.87 in the shallow North Sea, and 0.53 in the deep Norwegian Trench. The simulations in Figure 5 show no upstream bow wave system that is a characteristic of the wave generation of the critical Froude number range. Rather, upstream wave generation in the meteotsunami case occurs as free waves generated at the depth change between the shallow Norwegian Sea and the deep Norwegian Trench. The wave generation that occurs in the transcritical range where $Fr \sim 1$ is a qualitatively different, slow process taking place over long distances (e.g., Lee & Grimshaw, 1990; Li & Sclavounos, 2002; Pedersen, 1988; Torsvik et al., 2006; Wu, 1987).

We note that long precursor waves or free wave components of the wave wake due to fast or conventional ships have been observed without, however, identifying a proper generation mechanism (Didenkulova et al., 2011; Neumann et al., 2001; Parnell et al., 2007). The generation mechanism suggested here may provide an explanation of the measured wave amplitudes that are well in the linear regime, driven by the disturbance (ship) moving at subcritical speed. A similar mechanism appears at supercritical speed as well.

In this paper, we discuss and compare free wave generation at a localized, great depth change due to a passing (a) ship, or (b) thunderstorm. The waves are generated similarly in the two cases, where time and length scales differ. The ship tsunamis take place in Oslofjorden, Norway. The free wave generation process at a depth change is illustrated by fully dispersive mathematical model calculations and available wave radar measurements (Section 2). The meteotsunami case was generated by a supercell thunder storm that occurred on 29–30 June 2019. A short account on the driving weather is given. An idealized two-dimensional mathematical model is combined with three-dimensional calculations based on a realistic bathymetry and representation of the thunderstorm. Predictions are compared to available water-level measurements on the Norwegian Coast. The free wave generation in the meteotsunami case is compared to the ship case (Section 3). Summary points and conclusions are given in Section 4.

2. Free Wave Generation Due To a Ship

The purpose of this section is to describe the wave generation that occurs when a ship is moving past a great depth change. Despite the differences in time and length scale, the wave generation is similar in the meteotsunami case (Section 3).

2.1. Observations and Wave Radar Measurements

A moving ship forms a wave wake (e.g., Newman, 1977). At finite depth, at critical speed, in narrow channels, upstream nonlinear solitary waves are generated (e.g., Lee & Grimshaw, 1990; Li & Sclavounos, 2002; Pedersen, 1988; Torsvik et al., 2006; Wu, 1987). Here, we discuss a different kind of free wave generation. This is caused by a ship moving past a shallow, substantial depth change. The ship-driven small tsunamis in the Oslofjorden, Norway are a recent phenomenon (Grue, 2017). Color Fantasy and Color Magic, introduced in 2004 and 2007, respectively, are cruiseferries with a cardeck, and the world's largest of their kind. The waves emerge where the ships move past the shallow, great depth changes of the fjord. The ship speed is subcritical, and the wave front propagates with the shallow water speed, upstream of the ships. The wavelength is 0.5–1 km. The measured wave height on the shore has been up to 1.4 m (Figure 2d). The ship-driven small tsunamis pose a new erosion of the fjord (e.g., Parnell et al., 2007), hazard to public and maneuvering difficulties to other ships. Recently, the ship speed has been lowered, reducing also the wave impact.

The upstream waves are generated when the ship (Color Fantasy) is cruising across Ildjernsflu, a hot spot for the phenomenon. Ildjernsflu is a shallow region extending approximately 700 m along the ship track with a shallowest

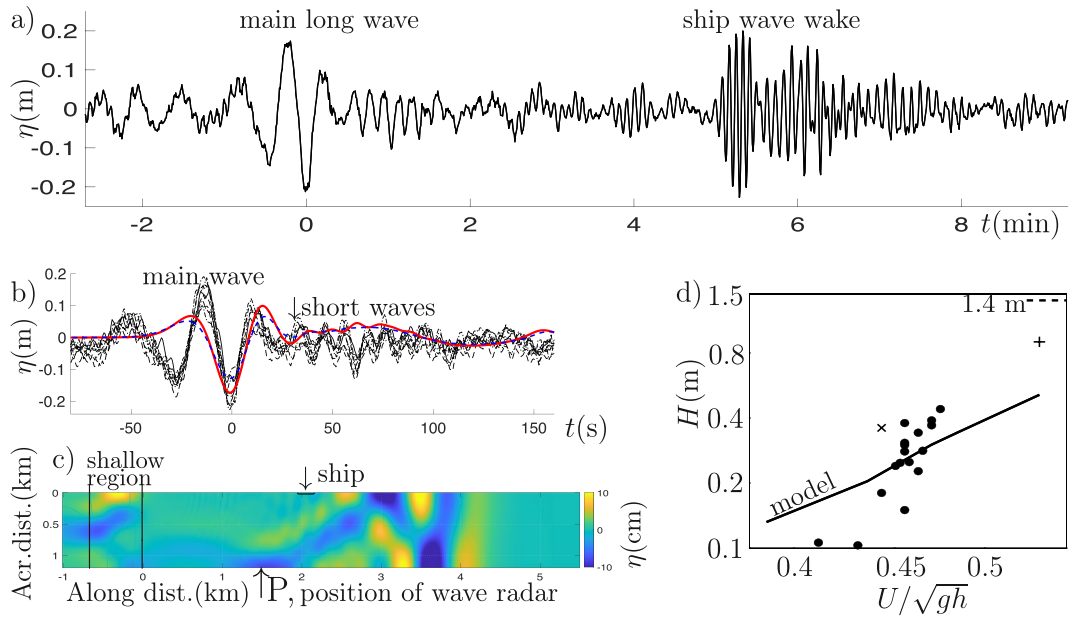

Figure 2. (a) Elevation due to Color Fantasy at speed 10 m/s, measured by the wave radar at Flaskebekk Pier on 29/10/2019. (b) Same for eight passages of the ship at speed ~9.6–10.1 m/s. Calculations using a model of Color Fantasy at 10 m/s (red solid), and a ship model with the same displacement, width and draught, with an unrealistically long bow and stern (blue dashed). $t = 0$ s refers to arrival time of the main trough. (c) Model calculation of the wave field. Ship at position 2.05 km upstream of the end of the shallow region at 0 km (d) Wave height H of main wave versus $U/\sqrt{gh}$ in log-log plot. Recordings from wave radar (•), video (×), photos (+), record wave height of 1.4 m – –, model computations (– – –).

depth of approximately 14 m. The depth before and after the shoal is 46 m, approximately. This implies a change $\Delta h = 32$ m of the water depth that is comparable to the average depth $\bar{h} = (14 + 46)/2\text{m} = 30$ m. The depth is quite uneven both across and along the shallow region. Color Fantasy is passing by the location every second day sometime between 9 and 10 a.m. Color Magic is passing by every other day but has changed to a route that avoids the main depth change, making only marginal waves. The ship to shore distance is approximately 1.2 km.

A wave radar of Miros (www.miros.com) was installed on the shore at Flaskebekk Pier. This is approximately 1.5 km upstream of the end of the Ildjernsflu shoal, measured along the ship track. A number of 17 elevation series due to Color Fantasy were measured by the wave radar during September–December 2019. Operating continuously, the radar provides the surface elevation twice per second. A record of 29 October 2019 exemplifies the dominant long wave arriving at the radar at 9.44 hr corresponding to time 9:26 (Figure 2a). The main crest is preceded by one deep trough and succeeded by another even deeper trough. The main trough is given a timing corresponding to $t = 0$ in the plots. Two estimates are made for the period: the elapsed time between the crests preceding and succeeding the main crest, divided by two (T_{CC}), and the trough-to-trough period (T_{TT}). For the case in Figure 2a, this obtains $T_{CC} = 29.8$ s while the trough-to-trough period of $T_{TT} = 27.5$ s is somewhat shorter. The maximum to minimum elevation is 0.39 m and the wave has a slope of 0.002, well in the linear regime. The ship wave wake arrives at the radar 5 min later. Color Fantasy was running at speed 10 m/s (19.4 kn) corresponding to a depth Froude number of $Fr = U/\sqrt{gh} = 0.471$ ($h = 46$ m), where the ship speed was obtained from www.marinetrafic.com.

Long waves of small amplitude appear in the measurements prior to the main wave (Figures 2a and 2b). These are generated by the ship interacting with the depth variations of the fjord, ahead of the main shallow region. The bottom topography of the water is in fact very uneven. A slight modification of the ship's track enhances or reduces the wave response (Figure 2d).

We focus on the main wave and calculations (Sections 2.2 and 2.3 below) are performed with an idealized model depth profile at Ildjernsflu. This has a constant depth of 46 m before the depth change, and then a gradual transition to a shallow, constant depth of 14 m, of length of 690 m. The depth then gradually increases to 46 m. The calculations using this model depth obtains the period and height of the main wave. The wave phase is only

Table 1
Speed U of Color Fantasy, Froude Number $U/\sqrt{gh}$ (h = 46 m), Measurements by the Wave Radar: Crest-to-Crest Period T_{CC}, Trough-to-Trough Period T_{TT}, Wave Height H, Date (Month, Date, Year) of Recording, Time of Exit From the Shoal

U(m/s)	$U\sqrt{gh}$	T_{CC}(s)	T_{TT}(s)	H(m)	YYYY/MM/DD	t(h)
8.75	0.413	28.5	29.9	0.106	2019/10/11	9.236
9.16	0.432	32.4	32.1	0.103	2019/10/13	9.200
9.41	0.444	34.5	28.4	0.180	2019/10/03	9.441
9.41[a]	0.444	–	–	0.360	2017/06/27	–
9.57	0.451	33.4	27.5	0.240	2019/12/02[C]	9.323
9.62	0.454	31.5	27.7	0.248	2019/10/27	9.426
9.67	0.456	27.8	27.8	0.150	2019/10/01	9.422
9.67	0.456	31.3	29.0	0.280	2019/11/02[C]	9.415
9.67	0.456	32.3	27.3	0.285	2019/10/31[C]	9.412
9.67	0.456	32.0	26.3	0.307	2019/11/30[C]	9.403
9.67	0.456	32.0	27.0	0.379	2019/11/06[C]	9.398
9.72	0.459	43.1	43.0	0.220	2019/10/25	9.416
9.83	0.463	32.1	28.8	0.227	2019/10/09	9.396
9.83	0.463	30.8	30.7	0.342	2019/11/24[C]	9.402
9.88	0.466	32.1	31.2	0.282	2019/11/04	9.406
9.88	0.471	30.3	29.6	0.370	2019/10/07	9.413
10.01	0.471	29.8	28.3	0.390	2019/10/29[C]	9.419
10.11	0.476	30.7	28.8	0.440	2019/11/26[C]	9.387
11.32[b]	0.533	–	–	0.900	2015/06/19/20	–

[a]Measured on the Shore by Video Camera and Ruler. [b]Estimated From Images of the Runup on the Shore. [C]Measurement series included in Figure 2b.

partially correct, however. In Figure 2b, a negative wave preceding the main trough is shown by the data sets but not by the model. This discrepancy is due to the differences between the depth in the fjord and the model depth. Work in progress includes records from two smaller ships running at smaller speeds. An interplay taking place between the ship length and the minor variations of the bottom topography is documented. A regression analysis of the wave response due to several ships is found to average out the short scale effects of the bottom variation (results are not shown). An improved depth matrix, to better calculate the measured waves, may depend on information that is beyond the available sea charts.

The period and height of the main wave obtained from the 17 radar elevation series are presented versus increasing ship speed (Table 1). The period T_{CC} is in the range between 28.8 and 43.1 s and T_{TT} in the range between 27 and 43 s. Averages over the radar measurements obtain $T = 32.0$ s and $T = 29.6$ s. As regards the wave response measured by the wave height, this has a range. For a fixed speed of $U = 9.7$ m/s (18.8 kn, $Fr = 0.456$), the measured wave height is between 0.150 and 0.379 m. This illustrates that the wave generation depends on the daily ship course. A small lateral shift along the uneven bottom produces a variation of the wave height. The table includes a wave height of 0.36 m, for a speed of 9.4 m/s (18.3 kn, $Fr = 0.44$), as obtained by video recording and a ruler mounted to a pole on the shore, next to the location of the wave radar. Another wave height of 0.9 m for speed of 11.3 m/s (22 kn, $Fr = 0.53$) was obtained from photos from 2015 in a bay nearby (Grue, 2017, 2020). In that bay, the record wave height of 1.4 m was measured. The ship speed at that event was not recorded. A complementary model calculation using a numerical wave tank of straight, vertical walls, and of an ideal model shallow region (Section 2.3) obtains a crest to crest period of 34 s ($U/\sqrt{gh} = 0.471$), which is close to the measurements. The computed wave height, fitting to the measured range, grows according to Fr^n with $n = 4.3$ (Figure 2d).

2.2. Modeling the Wave Making

We follow the mathematical model of Grue (2020). The water layer is bounded above by the free surface F and below by the bottom B. The ship geometry (or surface effect of pressure system) is specified by $z = \zeta_0(x - Ut, y) < 0$ where (x, y) are horizontal coordinates. The x-axis is directed along the motion direction. z is the vertical coordinate with $z = 0$ in the mean free surface, and t is the time. The ζ_0 corresponds to the barotropic effect of a moving storm. The bottom is specified by $z = -h + \beta(x, y)$ where h is a constant water depth, and the function β models the depth change. The formulation is fully dispersive. The fluid velocity (u, v, w) is evaluated by the gradient of the Laplacian potential ϕ. This is composed by the sum $\phi = \phi_0 + \psi$. The potential ϕ_0 models the steady velocity field attached to the ship or pressure system moving along a fluid layer of constant depth h. The ϕ_0 implies no vertical disturbance (waves) on the free surface, where in the present analysis, the short waves of the wave wake are not modeled. The potential ψ models the effect of the depth change. This includes the generation of the free waves.

The wave elevation η is integrated forward in time using a combination of the kinematic and dynamic free surface boundary conditions (see Grue, 2017, 2020). These are obtained in versions using the Fourier transform over the horizontal plane (e.g., Dahlquist & Björck, 1974, their chapter 9, Clamond & Grue, 2001, their Section 6):

$$\frac{\partial \hat{\eta}}{\partial t} - \hat{\psi}_F\,[k\tanh(kh)] = \frac{\hat{A}_1}{\cosh(kh)}, \tag{1}$$

$$\frac{\partial \hat{\psi}_F}{\partial t} + g\hat{\eta} = 0. \tag{2}$$

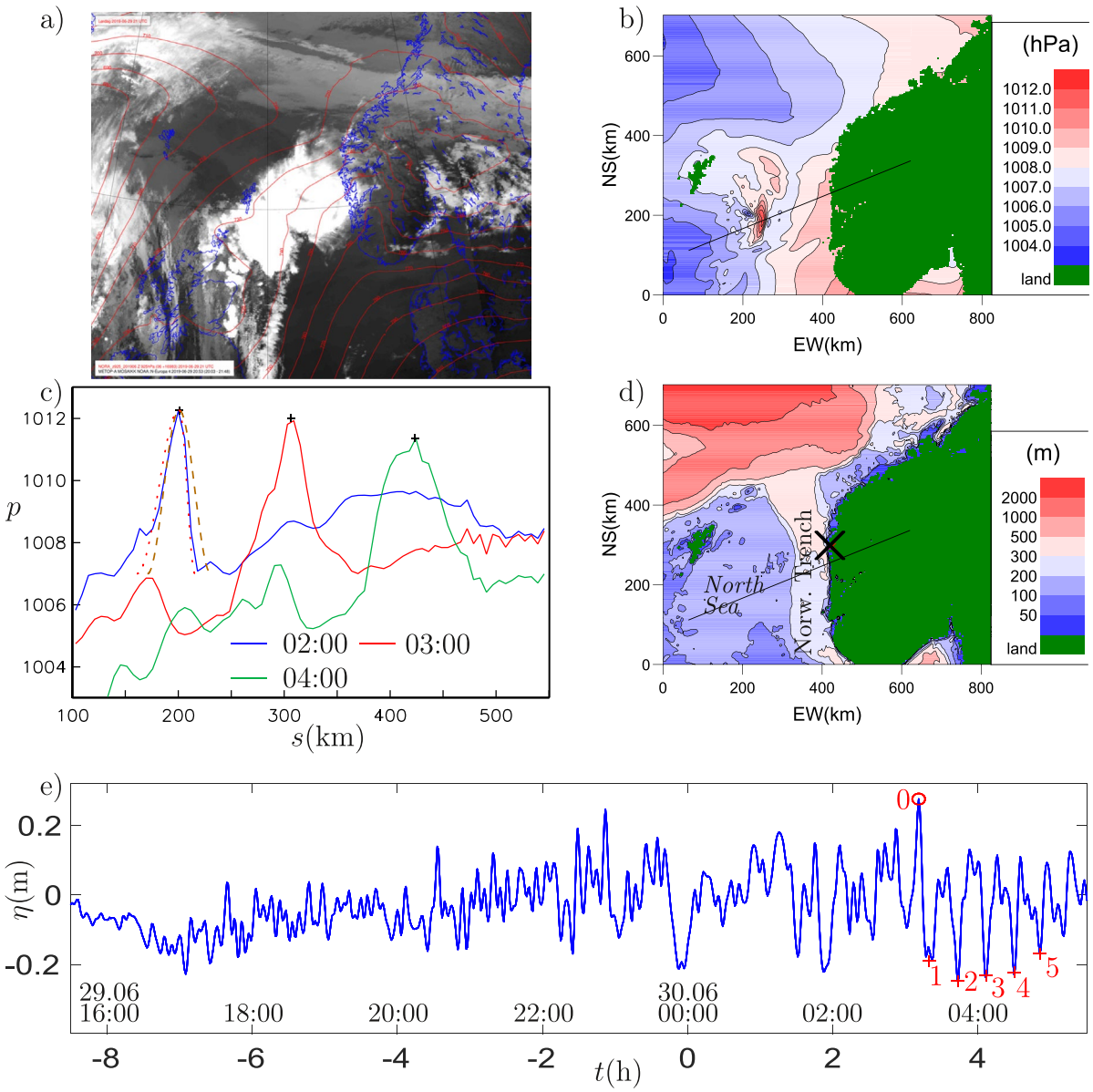

Figure 3. (a) Infrared satellite image from Eumetsat Metop C on 29 June, 20:53 UTC (22:53 CEST). Height of the 925 hPa surface (red solid line). (b) Pressure forecast on 30 June, 02:00 CEST. (c) Evolution of pressure (in bar) along transect. Estimated speed of local high pressure: 105.6 km/hr (between 02.00 and 03:00) and 117.1 km/hr (between 03:00 and 04:00). Long (symmetric) and short (asymmetric) dashes correspond to initial conditions for analytical solutions. (d) Bathymetry from ETOPO-1. The *North Sea* and The Norwegian Trench indicated. (e) Water level series at Byrknes (marked with × in plot d) made available by the Norwegian Mapping Authority.

Here, the index F denotes evaluation of ψ on the surface F. A hat denotes the Fourier transform in the horizontal plane, $\mathbf{k} = (k_x, k_y)$ the wavenumber vector in the Fourier domain and $k = |\mathbf{k}|$. The flux term A_1 due to the depth change is specified in Equation 3 below.

Equation 1 stems from $\eta_t = \partial\phi/\partial z$ on the surface. The vertical velocity is obtained by solution of the Laplace equation for the potential in the fluid volume. Expressed by use of Green's theorem and a Green function, the integral equation reads $\int_{F+B}(\phi G_n - G\phi_n)dS = -2\pi\phi'$, where index n denotes normal derivative pointing out of the fluid, and the evaluation point is at (x', y', z') on F or B (e.g., Newman, 1977). The two integral equations resulting from evaluation on the surface and the bottom are coupled. Notation $\phi = \phi(x, y, z)$ and $\phi' = \phi(x', y', z')$ are used. The Green function reads $G = 1/[(x - x')^2 + (y - y')^2 + (z - z')^2]^{1/2} + 1/[(x - x')^2 + (y - y')^2 + (2h + z + z')^2]^{1/2}$.

The integral equation on the free surface F obtains in Fourier transformed version: $(\widehat{\partial\phi/\partial z}) = \hat{\psi}_F\,[k\tanh(kh)] + \hat{A}_1/\cosh(kh)$, and $\hat{\phi}_{0,F}\,[k\tanh(kh)] = -U(\widehat{\partial\zeta_0/\partial x})$. The flux term

$$A_1 = \nabla_1\beta\cdot\nabla_1\phi_B + \beta\nabla_1^2\phi_B = -v_n \tag{3}$$

models the effect of the depth change. The index B denotes evaluation on the bottom B, and the variable A_1 represents a reaction velocity orthogonal to the bottom and is indicated by arrows 2 in Figures 1b and 1c. This is of equal magnitude and opposite direction of the ship-induced fluid velocity, v_n and is indicated by arrows 1. The sum $A_1 + v_n = 0$ at the impenetrable bottom. The vertical velocity $\mathcal{F}^{-1}[\hat{A}_1/\cosh(kh)]$ in Equation 1 corresponds to arrows 3 in Figures 1b and 1c ($\mathcal{F}^{-1}$ denotes inverse Fourier transform). This velocity is making the waves, and it is zero when there is no depth change and $\beta = 0$. In Equation 3, ∇_1 denotes horizontal gradient. The potential $\phi_B = \phi_{0,B} + \psi_B$ along the bottom is obtained by the integral equation evaluated at the bottom giving (in the Fourier transformed version): $k\hat{\phi}_B = k[\hat{\phi}_F - \mathcal{F}(\delta_0 V_F)]/\cosh kh - \hat{A}_1\tanh kh + k\hat{\mathcal{R}}$, where $V_F = -U\partial\delta_0/\partial x$ ($\mathcal{F}$ denotes the Fourier transform). The remainder $k\hat{\mathcal{R}}$ is accurately computed. Convergence is carefully checked.

2.3. Computations

Computations are performed with a numerical model wave tank of vertical walls. The width is twice the distance (of 1.2 km) between the ship track in the fjord and the shore. The model depth is $h = 46$ m. The shallow region is represented by $\beta(x, y) = 0.5\Delta h(\tanh[\alpha_0(x - x_a)] - \tanh[\alpha_0(x - x_b)])$ where $x_a = -0.69$ km, $x_b = 0$ km, $\Delta h = 32$ m, $\alpha_0 = 0.35$. A numerical model corresponding approximately to Color Fantasy is given by $\delta(x, y) = -d_0[1 - (2x/l_0)^8 - (2y/w_0)^6] < 0$, with (l_0, w_0, d_0) = (length, width, draught) = (210, 35, and 6.8 m). The displaced ship volume is 36,000 m^3.

The ship speed of 10 m/s (19.4 kn) corresponds to a depth Froude number of $U/\sqrt{gh} = 0.47$. The Froude number based on the ship length is $U/\sqrt{gl} = 0.22$. The free waves generated at the shallow region are visualized by the computation in Figure 2c. The longer upstream waves are followed by shorter waves. Waves are reflected from the shore where the computed elevation is compared to measurements by the wave radar, located 1.5 km upstream of the shallow region (indicated by letter P in Figure 2c). Eight of the measurement series (indicated in Table 1) is plotted together with a model computation for $U\sqrt{gh} = 0.471$. In the measurements, the ship speed was 9.6–10 m/s (18.6–19.6 kn, $U/\sqrt{gh}$ ~0.451–0.476). The measured wave height was 0.240 m $< H <$ 0.440 m. The computed H is between 0.255 and 0.304 m. The calculated elevation-trough-elevation wave has a period of 34 s, close to the measurements by the wave radar. The main trough is produced approximately 90 s prior to its arrival at the radar. The model computation of the dominant wave fits quite well to the recordings, although the depth of the actual fjord is far from constant, the shore is far from straight or parallel to the ship course, and the slope at the shore is finite.

2.4. Short Following Waves

A number of seven short crests appear between times of 30 and 103 s in the elevation series (Figure 2b). The average short wave period of 10 s corresponds to one third of the dominant wave period and is observed both in measurement (strong) and theory (weak). The short model waves are more pronounced for a somewhat higher speed. Another calculation using a ship of similar displacement but with an artificially long bow and stern, where the gradients of the bow and stern are strongly reduced, exhibits the same leading wave system, although of a weaker amplitude, but no short waves. This suggests that the short following waves in Figure 2b may be generated by the bow and stern of the ship. This illustrates that gradients and short scale effects of a moving pressure system may generate both long and short waves (see the dashed blue line in the figure).

Finally, the radar measurements and model calculations of the small ship-induced tsunamis show corresponding: (a) period of the main wave, (b) height of the main wave, for the similar Froude number, and (c) short following waves of period of 1/3 of the main wave.

3. Meteotsunami on 29–30 June 2019

3.1. Background and Observations

We now discuss free wave effects in the meteotsunami event that occurred on the Norwegian Coast on 29–30 June 2019. The main meteorological contribution to sea-level variations of the Norwegian waters is caused by mid-latitude low pressure systems. These are cyclones generated as instabilities on the Polar front, generally located between 40 and 70° north. The typical horizontal length scale of these is approximately 2000 km, usually referred to as the synoptic scale. However, meso-scale weather systems with typical horizontal length scale of the order of 100 km, and corresponding oscillations in the atmospheric pressure, may induce rapid changes in the water level. A sudden atmospheric pressure drop of say 5 hPa will generate a barotropic wave approximately 5 cm high propagating toward the coast where it may be amplified by shallow water effects.

In the evening of 29 June, a system of convective clouds were developing over the Scottish highland. The clouds were advected toward the north east by the south-westerly winds at the time. Figure 3a shows an image from the Eumetsat Metop C satellite taken at approximately 21:00 UTC. Metop C observes the infra-red part of the spectrum at 11 μm. White shows the areas with very low temperatures, indicating cloud tops. The solid red lines are the height of the 925 hPa surface, which shows the pressure distribution at around 800 m above the ground, taken from the meteorological hindcast archive at MET Norway (Reistad et al., 2011). This is the approximate height of the planetary boundary layer, above which the atmospheric flow is generally regarded to be in geostrophic balance (Linders & Saetra, 2010). The most intense white area between Scotland and Shetland has cloud top temperatures down to approximately −60°C, indicating deep convection all the way up to the tropopause. This is a massive deep-convective cloud penetrating the entire troposphere and is generally referred to as a supercell thunderstorm (Holton, 2004; Klemp, 1987). The supercell (composed by several convective cells) covered the entire ocean between the Orkney Islands, Shetland and the west-coast of Norway, at this time.

A water level recording at Byrknes on the Norwegian Coast, made available from the Norwegian Mapping Authority, illustrates the meteotsunami response due to the storm. Byrknes, located right south of the mouth of Sognefjorden, is marked by the cross in Figure 3d, approximately in the middle. A transition from calm to fluctuating water level is observed on 29 June at 17:00 CEST (Central European Summer Time, equal to UTC+02:00; Figure 3e). Two oscillations, each approximately of 1-hr duration, occurred between 22:00 and 24:00. Oscillations of period of barely 0.4 hr and height of up to 0.5 m are identified between 03:00 and 05:00 in the morning of 30 June. According to the witness observations, the meteotsunami caused severe damage in the village of Byrknes at 03:30 in this morning. Another water level record obtained at Skjolden, the innermost location of the Sognefjorden, documents strong fluctuations between 19:00 on 29 June and 06:00 on 30 June 06:00. A dominant period of approximately 1 hr and oscillation height of up to 0.8 m occurred in the morning of 30 June (results not shown). Available observation records of the mean sea-level pressure at the Troll C platform in the North Sea, obtained every 10 min, exhibit rapid oscillations from 18:00 on 29 June and onwards. The fluctuations were obviously induced by the turbulent vertical motion of air within the convective cloud cells (results not shown).

4. Mathematical Modeling

4.1. Long Wave Approximations

We model the wave effects in the meteotsunami including the response on the coast, in the morning of 30 June. The geometries of the fjords are not resolved, and we do not calculate the motion there. The mathematical modeling necessarily begins with the driving weather. Figure 3b shows the mean sea-level pressure at 02:00 on 30 June, as obtained from the forecasting system operated by the Norwegian Meteorological Institute (Müller et al., 2017). The part of the storm moved rapidly toward the coast of Norway and made landfall near the mouth of Sognefjorden some time between 03:00 and 04:00 on 30 June, and faded quite rapidly after that. At 02:00 the thunderstorm structure had a width of 60 km. It propagated along the line shown in Figure 3b with a speed above 100 km/hr, while widening somewhat. Pressure transects are shown in Figure 3c. The speed and width of the pressure structure induced a surface depression with period of about a half of an hour. This increased substantially as the structure approached land. At 02:00, the pressure moved across an ocean depth of approximately 115 m. Later, it crossed the Norwegian Trench with the water depth down to 300 m. The depth change of $\Delta h = 185$ m is comparable the average depth of $\bar{h} = (115 + 300)/2$ m $= 208$ m. The speed of the pressure system corresponds

to local Froude numbers (relative to the shallow water speed $\sqrt{gh}$) ranging from 0.87 to 0.53, which are rather large, but still subcritical.

Even though the thunderstorm is a comparatively small meteorological feature it still has very large horizontal extent compared to the relevant water depths, which is a few hundred meters or less. Hence, linear shallow water theory is adequate for the analysis of the sea surface response (the dispersive mathematical model in Section 2.2 is not effective on the scale of the meteotsunami). The continuity equation reads

$$\frac{\partial \eta}{\partial t} = -\nabla \cdot (h\mathbf{u}) - \frac{\partial h}{\partial t}, \tag{4}$$

where η is the surface elevation, h ocean depth, and $\mathbf{u}$ is the horizontal velocity. This is taken as uniform in the vertical direction. The time-dependent bottom may represent wave generation by a submarine slide (e.g., Didenkulova et al., 2010; Løvholt et al., 2015; Tinti et al., 2001) and is included in the equation for completeness, see the discussion below Equation 5. Introducing a surface pressure, p, the momentum equation reads

$$\frac{\partial \mathbf{u}}{\partial t} = -g\nabla\eta - \frac{1}{\rho}\nabla p + \frac{\mathbf{d}}{\rho h} - f\mathbf{i_z} \times \mathbf{u}, \tag{5}$$

where $\mathbf{d}$ is a parameterized vector drag on the surface due to wind and f is the Coriolis parameter. $\mathbf{i_z}$ is vertical unit vector. When the depth is split according to $h \to h(x, y) + H_0(x, y, t)$, where the time-dependent part H_0 is much smaller than h, we may transform Equations 4 and 5 to the corresponding set, without the time derivative of the depth in the continuity equation, through $\eta \to \eta + H_0$ and $p \to p - \rho g H_0$. Hence, while an equivalent ($p = -\rho g H$) forcing from the bottom or the surface make a simple difference for the surface elevation, the velocity fields are the same. To a large degree this is conveyed also into nonlinear and weakly dispersive theory (e.g., Pedersen, 1988). For sources with length scales comparable to the depth there are, however, significant differences. A source at the bottom produces a surface response of larger horizontal extent, see Løvholt et al. (2015) and references therein.

Herein, rotational effects are of minor importance and are omitted. Moreover, using the forecast values for the wind and a drag coefficient of 2.3×10^{-3} (Thiebaut & Vennell, 2011) we estimate the wind effect to be small. Hence, it is neglected. When a pressure field of permanent shape propagates over constant bottom, with a constant speed U in the x-direction, relations 4 and 5 imply a Poisson-type equation for a stationary response

$$(1 - Fr^2)\frac{\partial^2 \eta}{\partial \xi^2} + \frac{\partial^2 \eta}{\partial y^2} = -\frac{1}{\rho g}\nabla^2 p, \tag{6}$$

where $\xi = x - Ut$ and $Fr = U/\sqrt{gh}$ (Froude number). Equations of this type, with extensions (wind, rotation), are elaborately discussed in, for example, Thiebaut and Vennell (2011). Herein, the Poisson equation is solved numerically by standard software FISHPACK (see the reference to Adams et al., 2016). Below, we will employ surface pressures of finite horizontal extent. Then, for finite, but subcritical, Froude numbers the η determined from Equation 6 will generally extend way beyond the pressure region (Figure 4c). If a sudden onset of the pressure field is assumed, the total solution is the sum of the stationary forced solution, given by Equation 6, and the free waves. The latter corresponds to the solution of the initial value problem where the forced solution, with a minus sign, is used for initiation. When Fr is fairly close to 1, a long time is required before the forced part of the solution becomes dominant. This has implications for discussions below.

4.2. Plane Case

In the plane case, there is a basic solution of Equation 6 that will be used in an idealized analysis below:

$$\eta = -\frac{p}{\rho g(1 - Fr^2)}, \quad u = Fr\sqrt{\frac{g}{h}}\eta. \tag{7}$$

The velocity, u, is reduced by factor Fr as compared to the velocity of a free wave with an elevation of the same shape and height. Hence, when the forced wave encounters an impermeable wall, which may serve as a crude representation of a steep coast, the reflected free wave will have an amplitude reduced by the factor Fr as compared to the incident, forced wave.

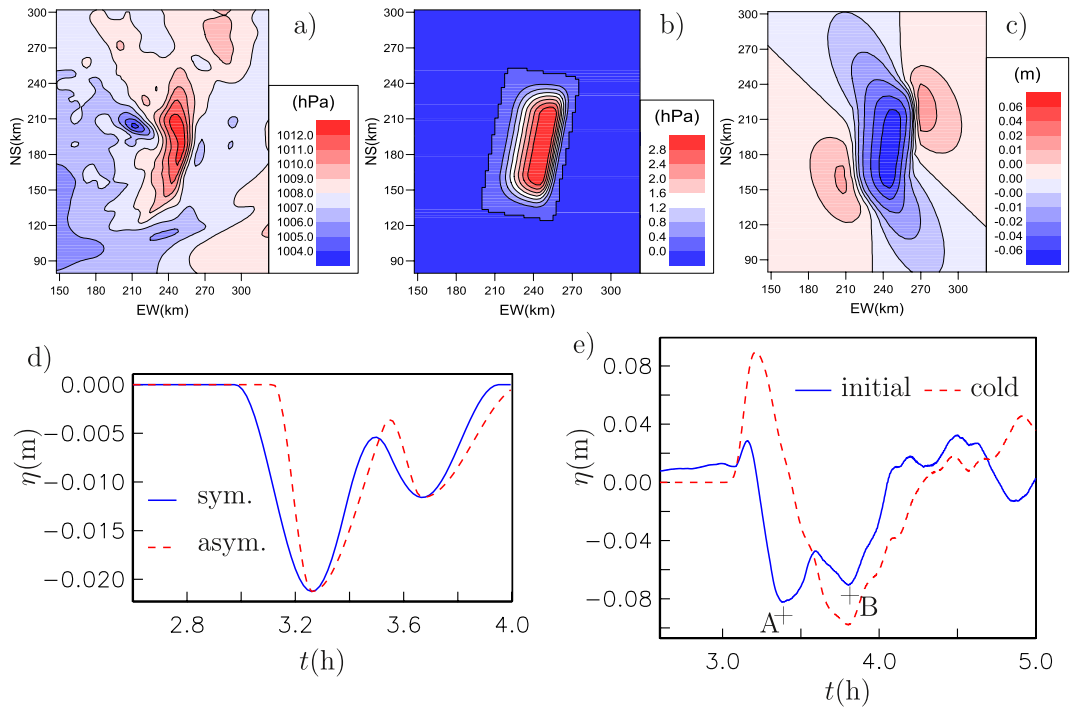

Figure 4. (a) pressure structure from forecast. (b) Idealized pressure structure. (c) Stationary surface response. (d) Analytic time series. (e) Elevation time series off Byrknes for the different initial conditions. + marks first (a) and second (b) minima with simulation "initial.".

The meteotsunami that occurred in the morning of 30 June 2019 is analyzed for an idealized pressure structure of constant shape following the transect in Figures 3b and 3d at a speed of 105.6 km/hr. The pressure from the forecast and the idealized ones are shown in Figures 3b, 3c, 4a and 4b. For illustration purposes, plane (two-dimensional) analytical solutions relating to the trajectory of the thunderstorm are sought. Following Vennell (2007), we replace the North Sea plateau and the Norwegian Trench with regions of constant depths (115 and 294 m respectively), the steep coast with a vertical wall, and patch local solutions at the step and the wall. The local solutions are either forced solutions, as given by Equation 7, or free solutions with similar shape and temporal duration (period). In the trench a free transmitted depression, with an amplitude that is 40% higher than the forced one, is generated. The two waves will be partly separated before they reach the coast. As a consequence the time series at the coast displays two troughs. The first one, arriving at 3.27 hr (03:16) is the deepest and is related to the free wave (Figure 4d). The one that is due to the forced depression is less strong, arriving at 3.67 hr (03:40). The separation time between the troughs, of 24 min (0.4 hr), corresponds quite well to the period of 23 min between the marked depressions of the measurements, number one and two, occurring at 03:20 and 03:43, respectively (Figure 3e).

4.3. Comparison to Water Level Recordings

The simulations (using the model from Løvholt et al., 2008) are compared to the water level recordings (Figure 3e). The gauge is located at 79 m depth, a few km offshore of the village of Byrknes (cross in Figure 3d). The wave effects that appeared at the Norwegian coast from 03:00 on 30 June and onwards have been calculated (Figure 5). The free wave elevation transient, driven by the abrupt onset of the pressure feature at the Scottish coast, results in a calculated elevation maximum at the location of Byrknes at 03:13 (Figure 4e). Next arrives the free depression wave, generated at the depth transition between the North Sea and the Norwegian Trench, resulting in a calculated elevation minimum at Byrknes at 03:24 (3.40 hr, marked with +A in Figure 4e). 24 Min (0.4 hr) later, the forced wave gives a second minimum of the calculated elevation at Byrknes (marked with +B). The elevation series from the wave gauge shows, for the time window between 03:00 and 05:00, first, a strong elevation maximum occurring at time 03:11. This is marked with a circle and a number 0 (Figure 3e). Next, a number of

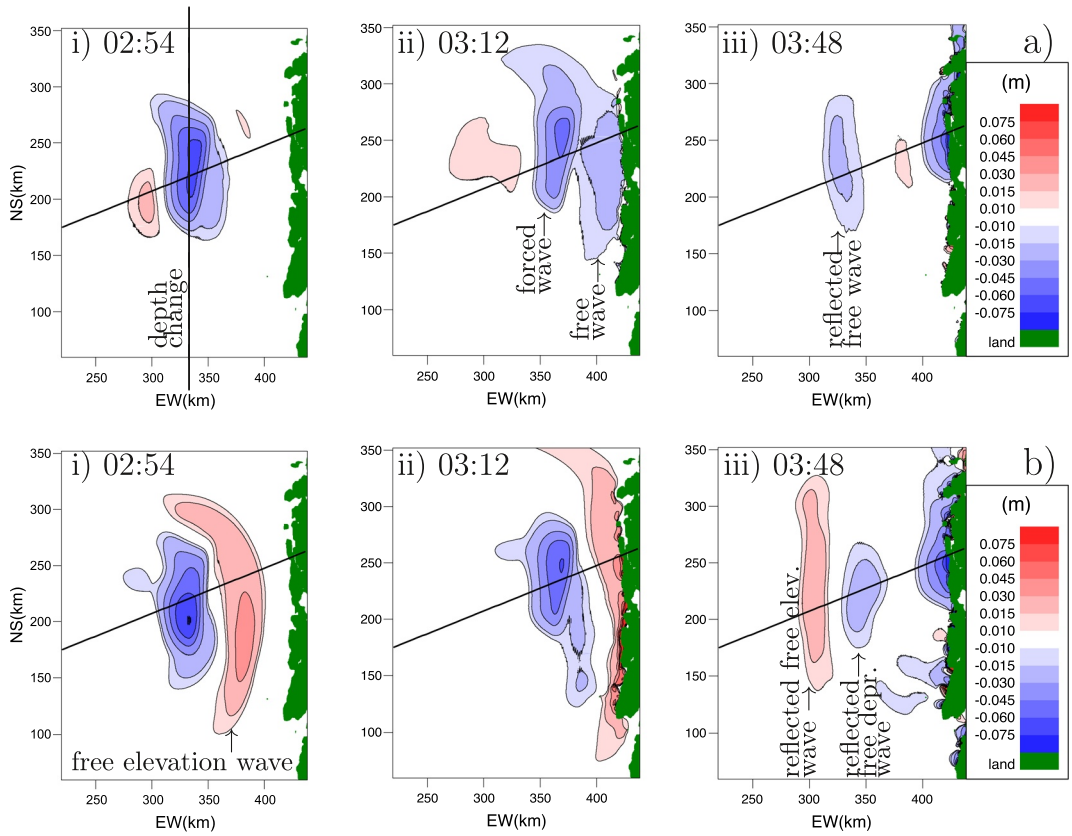

Figure 5. Simulations of free wave effects. (a) Complete initiation of forced wave, "initial." (b) Start from rest, "cold." Times 02:54, 03:12, 03:48 hr on 30.06.

five elevation minima occur at times 03:20, 03:43, 04:07, 04:30, 04:51. These are indicated by crosses and numbers 1–5. The timing of the simulated wave effects corresponds rather well to the measured elevation maximum marked by number 0, and to the minima, marked by numbers 1 and 2. This includes the wave transient due to the "cold start". The calculated separation time of 24 min between depressions marked by 1 and 2 corresponds rather well to the average period of approximately 23 min, of the sequence of the measured elevation minima.

The calculated amplitudes (of the 23 min oscillations) are less than those observed in the water level recordings. In the observations, the amplitude of these periods may have been strongly enhanced by resonant response in the coastal geometry. In the computations, the numerical grid is too coarse to reproduce such effects. The grid resolution of 995 m (6 mill. grid points) resolves well the offshore regions, while the coastal waters are not represented in any detail, however.

Besides the dominant oscillations, the water level recordings exhibit systematically short wave effects of oscillation period of 6–7.5 min. This period range corresponds to 0.002–0.003 Hz and is close to the infra gravity wave range. Such short waves are not present in the calculations. This is probably due to the application of an idealized and smooth atmospheric forcing model. The high oscillation period may originate from short scale effects of the driving weather that were not included in the weather forecast as used in the present simulations.

4.4. Ship- and Meteotsunami Compared

At this point, we may compare the free wave generation at the depth transition in the two cases, the ship and the meteotsunami. The depth change Δh is comparable to the average depth $\bar{h}$ in both cases. For the ship, the wavelength is 640 m while the water depth outside the shallow region is 46 m, giving a nondimensional wavenumber of $kh = 0.45$. The leading wavelength is observed to increase with the propagation distance (Grue, 2017). Above the shallow and deep regions the Froude number is 0.85 and 0.48, respectively. The ship is elongated in the travel

direction. The wave response measured by the wave height of the main wave grows with the ship speed to a power of 4.3. In the meteotsunami case the driving pressure is elongated in the transverse direction and the wavelength is 50 km, while the water depth in the Norwegian Trench is 300 m, giving a nondimensional wavenumber of $kh = 0.038$. This is a factor 1/12 smaller than the ship case. The Froude numbers in the meteotsunami case are 0.87 and 0.53 in the North Sea and the Norwegian Trench, respectively, and are similar to those in the ship case.

In the ship case, an additional series of short waves of period 1/3 of the main wave(s) may originate from the steep gradients of the bow and stern. The short waves were obtained both in measurement (strong) and calculation (weak). Similar short wave effects are indeed observed in the time series of the water-level measurement in the meteotsunami case, although the direct cause is not identified (Figure 3e). The modeling of the meteotsunami did not reproduce the short waves. This may suggest that the short effects of the driving weather were not resolved by the weather forecast used as input to the present calculations.

5. Summary and Conclusion

We have investigated free wave generation due to pressure systems moving across substantial depth changes of the water. The first case concerns a ship moving along a shallow waterway (the forcing by a ship may well be represented by a pressure distribution). The second is a meteotsunami that occurred on the Norwegian Coast on 29–30 June 2019 for which the driving weather moved across the shallow depth transition between the North Sea and the deep Norwegian Trench. The wave response is measured on the shore (coast) in both cases. Both cases are modeled mathematically and are illustrated and interpreted by numerical computations.

The wave generation mechanism is presented in its very detail in the ship case. At the depth transition, the forced wave and velocity field attached to the moving pressure system adjust to the new depth. The free wave is generated during the transition process between the two different water depths. The depth change is comparable to the average water depth in both cases ($\Delta h \sim \bar{h}$).

The wavenumber of the free waves is a factor 1/12 smaller in the meteotsunami case compared to that of the ship. Essential wave dispersion in the ship case is observed. The subcritical depth Froude numbers are similar in the two cases. The wave response measured by the wave height grows with the ship speed to a power of 4.3.

The meteotsunami that occurred on the Norwegian Coast on 29–30 June 2019 was driven by a supercell thunderstorm moving rapidly from the north of Scotland toward Norway. The water-level response, as measured on the Norwegian Coast, showed a transition from calm to fluctuating state on 29 June at 19:00, and a longer series of relatively regular oscillations of period of scant 0.4 hr in the morning of 30 June. Eyewitnesses living next to the location of the water-level gauge reported on the storm and the violent long wave event occurring from 03:30 and onwards in the morning of 30 June. The long waves caused severe damage.

The mean sea-level pressure in the morning of 30 June, obtained from the forecasting system at the Norwegian Meteorological Institute, shows a localized, strong high pressure feature of width of approximately 60 km and crest of approximately 120 km, moving toward the Norwegian Coast at a speed of 100–120 km/hr. This pressure system has been used as input for a set of simulations of the sea-level response including realistic bathymetry, however, without resolving the details of the coastal topography and fjord systems. The calculations demonstrate that a free depression wave was generated as the storm passed by the transition between the North Sea and the Norwegian Trench. The forerunning free trough arrived at the coast 24 min ahead of the depression attached to the storm. This calculation is very close to reproduce an observed period of 23 min, of a series of five oscillations of height of 0.3–0.4 m that occurred between 03:00 and 05:30 in the morning of 30 June. The simulations suggest that the combination of the free and forced waves triggered a local resonant mode of the local coastal bathymetry. Two different initial conditions were investigated, either with a pre-calculated forced wave, or a sudden start from rest. The latter case generates a forerunning transient upstart elevation wave in addition to the depression wave at the Norwegian Trench. The scenario implied by an abrupt start from rest may be relevant, since the storm on 29–30 June had a rapid interaction with the waters north of Scotland. The timing of the forerunning elevation at the coast may fit with a strong, measured elevation in the water-level recordings.

For both the ship case and the meteotsunami case, short wave effects were observed. In the ship case, short waves of period 1/3 of the main waves may originate from the steep gradients of the bow and stern of the ship, as obtained both in measurement and computation. As for the meteotsunami case, short waves of period 6–7.5 min

(0.002–0.003 Hz) are evident in the time series of the water-level measurement on the coast. The short waves may originate from the driving weather, where the weather forecast used in the present simulations did not have such short scale effects. The short wave frequencies fit with the range of infra gravity waves.

Data Availability Statement

The files of the time series of the wave radar, the water-level time series at Byrknes and the pressure forecast in Figures 3b and 3c are available on https://dataverse.no.

Acknowledgments
We thank Dr. Kai H. Christensen of MET Norway for providing the forecast of the sea-level pressure and Jonas Røstad and Gunnar Prytz of Miros for sending wave radar data files. Tore Henning Larsen and J.G. registered passage time and speed of Color Fantasy. Dr. Ira Didenkulova is thanked for comments and suggestions.

References

Adams, J. C., Swarztrauber, P. N., & Sweet, R. (2016). *FISHPACK: Efficient Fortran subprograms for the solution of separable elliptic partial differential equations*. Retrieved from https://www2.cisl.ucar.edu/resources/legacy/fishpack

Chen, Y., & Niu, X. (2018). Forced wave induced by an atmospheric pressure disturbance moving towards shore. *Continental Shelf Research*, *160*, 1–9. https://doi.org/10.1016/j.csr.2018.03.007

Clamond, D., & Grue, J. (2001). A fast method for fully nonlinear water wave computations. *Journal of Fluid Mechanics*, *447*, 337–355. https://doi.org/10.1017/S0022112001006000

Dahlquist, G., & Björck, Å. (1974). *Numerical methods* (p. 573). Prentice-Hall.

Didenkulova, I., Nikolkina, I., Pelinovsky, E., & Zahibo, N. (2010). Tsunami waves generated by submarine landslides of variable volume: Analytical solutions for a basin of variable depth. *Natural Hazards and Earth System Sciences*, *10*, 2407–2419. https://doi.org/10.5194/nhess-10-2407-2010

Didenkulova, I., Pelinovsky, E., & Soomere, T. (2011). Can the waves generated by fast ferries be a physical model of tsunami? *Pure and Applied Geophysics*, *168*, 2071–2082. https://doi.org/10.1007/s00024-011-0289-z

Dogan, G. G., Pelinovsky, E., Zaytsev, A., Metin, A. D., Tarakcioglu, G. O., Yalciner, A. C., et al. (2021). Long wave generation and coastal amplification due to propagating atmospheric pressure disturbances. *Natural Hazards*, *106*, 1195–1221. https://doi.org/10.1007/s11069-021-04625-9

Grue, J. (2017). Ship generated mini-tsunamis. *Journal of Fluid Mechanics*, *816*, 141–166. https://doi.org/10.1017/jfm.2017.67

Grue, J. (2020). Mini-tsunami made by ship moving across a depth change. *Journal of Waterways, Port, Coastal, and Ocean Engineering*, *146*(5), 04020023. https://doi.org/10.1061/(ASCE)WW.1943-5460.0000585

Holton, J. R. (2004). *An introduction to dynamical meteorology, International Geophysics Series* (Vol. 88). London, UK: Elsevier Academic Press.

Klemp, J. B. (1987). Dynamics of tornadic thunderstorms. *Annual Review of Fluid Mechanics*, *19*, 369–402. https://doi.org/10.1146/annurev.fl.19.010187.002101

Lee, S.-J., & Grimshaw, R. H. J. (1990). Upstream-advancing waves generated by three-dimensional moving disturbances. *Physics of Fluids*, *A2*(2), 194–201. https://doi.org/10.1063/1.857769

Linders, T., & Saetra, Ø. (2010). Can cape maintain polar lows? *Journal of the Atmospheric Sciences*, *67*, 2559–2571. https://doi.org/10.5194/nhess-6-1035-2006

Li, Y., & Sclavounos, P. D. (2002). Three-dimensional nonlinear solitary waves in shallow water generated by an advancing disturbance. *Journal of Fluid Mechanics*, *470*, 383–410. https://doi.org/10.1017/S0022112002001568

Løvholt, F., Pedersen, G. K., & Gisler, G. (2008). Oceanic propagation of a potential tsunami from the La Palma Island. *Journal of Geophysical Research*, *113*, C09026. https://doi.org/10.1029/2007JC004603

Løvholt, F., Pedersen, G. K., Harbitz, C. B., Glimsdal, S., & Kim, J. (2015). On the characteristics of landslide tsunamis. *Philosophical Transactions of the Royal Society A: Mathematical, Physical and Engineering Sciences*, *373*, 20140376. https://doi.org/10.1098/rsta.2014.0376

Mercer, D., Sheng, J., Greatbatch, R. J., & Bobanovic, J. (2002). Barotropic waves generated by storms moving rapidly over shallow water. *Journal of Geophysical Research*, *107*(C10), 1–16. https://doi.org/10.1029/2001JC001140

Monserrat, S., Vilibić, L., & Rabinovich, A. B. (2006). Meteotsunamis: Atmospherically induced destructive ocean waves in the tsunami frequency band. *Natural Hazards and Earth System Sciences*, *6*, 1035–1051. https://doi.org/10.5194/nhess-6-1035-2006,2006

Müller, M., Homleid, M., Ivarsson, K.-I., Køltzow, M. A. Ø., Lindskog, M., Midtbø, K. H., et al. (2017). Arome-metcoop: A nordic convective-scale operational weather prediction model. *Weather and Forecasting*, *32*, 609–626. https://doi.org/10.1175/WAF-D-16-0099.1

Neumann, D. G., Tapio, E., Haggard, D., Laws, K. E., & Bland, R. W. (2001). Observations of long waves generated by ferries. *Canadian Journal of Remote Sensing*, *27*(4), 361–370. https://doi.org/10.1080/07038992.2001.10854878

Newman, J. N. (1977). *Marine hydrodynamics* (p. 402). MIT Press.

Niu, X., & Zhou, H. (2015). Wave pattern induced by a moving atmospheric pressure disturbance. *Applied Ocean Research*, *52*, 37–42. https://doi.org/10.1016/j.apor.2015.05.003

Parnell, K. E., McDonald, S. C., & Burke, A. E. (2007). Shoreline effects of vessel wakes, Marlborough Sounds, New Zealand. *Journal of Coastal Research*, *50*, 502–506. Retrieved from https://www.jstor.org/stable/26481640

Pattiaratchi, C. B., & Wijeratne, E. M. S. (2015). Are meteotsunamis an underrated hazard? *Philosophical Transactions of the Royal Society A*, *373*, 20140377. https://doi.org/10.1098/rsta.2014.0377

Pedersen, G. K. (1988). Three-dimensional wave patterns generated by moving disturbances at critical speeds. *Journal of Fluid Mechanics*, *196*, 39–63. https://doi.org/10.1017/S0022112088002605

Rabinovich, A. B. (2020). Twenty-seven years of progress in the science of meteorological tsunamis following the Daytona Beach event. *Pure and Applied Geophysics*, *177*(3), 1193–1230. https://doi.org/10.1007/s00024-019-02349-3

Reistad, M., Breivik, Ø., Haakenstad, H., Aarnes, O. J., Furevik, B. R., & Bidlot, J. R. (2011). A high-resolution hindcast of wind and waves for the north sea, the Norwegian sea, and the Barents sea. *Journal of Geophysical Research: Oceans*, *116*(C5), 1–18. https://doi.org/10.1029/2010JC006402

Satake, K., & Atwater, B. F. (2007). Long-term perspectives of giant earthquakes and tsunamis at subduction zones. *Annual Review of Earth and Planetary Sciences*, *35*, 349–374. https://doi.org/10.1146/annurev.earth.35.031306.140302

Šepić, J., Vilibić, I., Rabinovich, A. B., & Tinti, S. (2018). Meteotsunami ("Marrobbio") of 25–26 June 2014 on the Southwestern coast of Sicily, Italy. *Pure and Applied Geophysics*, *175*, 1573–1593. https://doi.org/10.1007/s00024-018-1827-8

Thiebaut, S., & Vennell, R. (2011). Resonance of long waves generated by storms obliquely crossing shelf topography in a rotating ocean. *Journal of Fluid Mechanics*, *682*, 261–288. https://doi.org/10.1017/jfm.2011.221

Tinti, S., Bortolucci, E., & Chiavettieri, C. (2001). Tsunami excitation by submarine slides in shallow-water approximation. *Pure and Applied Geophysics*, *158*, 759–797. https://doi.org/10.1007/PL00001203

Torsvik, T., Dysthe, K., & Pedersen, G. K. (2006). Influence of variable Froude number on waves generated by ships in shallow water. *Physics of Fluids*, *18*, 062102. https://doi.org/10.1063/1.2212988

Vennell, R. (2007). Long barotropic waves generated by storm crossing topography. *Journal of Physical Oceanography*, *37*, 2809–2823. https://doi.org/10.1175/2007JPO3687.1

Vilibić, I., Rabinovich, A. B., & Anderson, E. J. (2021). Special issue on the global perspective on meteotsunami science: Editorial. *Natural Hazards*, *106*, 1087–1104. https://doi.org/10.1007/s11069-021-04679-9

Wu, T. Y. (1987). Generation of upstream advancing solitons by moving disturbances. *Journal of Fluid Mechanics*, *184*, 75–99. https://doi.org/10.1017/S0022112087002817